LJMU Research Online

Bossini, D, Miglio, A, Salaris, M, Vrard, M, Cassisi, S, Mosser, B, Montalban, J, Girardi, L, Noels, A, Bressan, A, Pietrinferni, A and Tayar, J

 Kepler red-clump stars in the field and in open clusters: Constraints on core mixing

http://researchonline.ljmu.ac.uk/id/eprint/13205/

Article

Kepler red-clump stars in the field and in open clusters: constraints on core mixing

D. Bossini,[1,2]★ A. Miglio,[1,2] M. Salaris,[3] M. Vrard,[4] S. Cassisi,[5] B. Mosser,[6] J. Montalbán,[7] L. Girardi,[8] A. Noels,[9] A. Bressan,[10] A. Pietrinferni[5] and J. Tayar[11]

[1]*School of Physics and Astronomy, University of Birmingham, Edgbaston, Birmingham B15 2TT, UK*
[2]*Stellar Astrophysics Centre, Department of Physics and Astronomy, Aarhus University, Ny Munkegade 120, DK-8000 Aarhus C, Denmark*
[3]*Astrophysics Research Institute, Liverpool John Moores University, 146 Brownlow Hill, Liverpool L3 5RF, UK*
[4]*Instituto de Astrofísica e Ciências do Espaço, Universidade do Porto, CAUP, Rua das Estrelas, 4150-762 Porto, Portugal*
[5]*Osservatorio Astronomico di Collurania – INAF, via M. Maggini, I-64100 Teramo, Italy*
[6]*LESIA, Observatoire de Paris, PSL Research University, CNRS, Université Pierre et Marie Curie, Université Paris Diderot, F-92195 Meudon, France*
[7]*Dipartimento di Fisica e Astronomia, Università di Padova, Vicolo dell'Osservatorio 3, I-35122 Padova, Italy*
[8]*Osservatorio Astronomico di Padova – INAF, Vicolo dell'Osservatorio 5, I-35122 Padova, Italy*
[9]*Institut d'Astrophysique et Géophysique de l'Université de Liège, Allée du six Août, 19c B-4000 Liège, Belgium*
[10]*SISSA, via Bonomea 265, I-34136 Trieste, Italy*
[11]*Department of Astronomy, Ohio State University, 140 W 18th Ave, OH 43210, USA*

ABSTRACT

Convective mixing in helium-core-burning (HeCB) stars is one of the outstanding issues in stellar modelling. The precise asteroseismic measurements of gravity-mode period spacing ($\Delta\Pi_1$) have opened the door to detailed studies of the near-core structure of such stars, which had not been possible before. Here, we provide stringent tests of various core-mixing scenarios against the largely unbiased population of red-clump stars belonging to the old-open clusters monitored by *Kepler*, and by coupling the updated precise inference on $\Delta\Pi_1$ in thousands of field stars with spectroscopic constraints. We find that models with moderate overshooting successfully reproduce the range observed of $\Delta\Pi_1$ in clusters. In particular, we show that there is no evidence for the need to extend the size of the adiabatically stratified core, at least at the beginning of the HeCB phase. This conclusion is based primarily on ensemble studies of $\Delta\Pi_1$ as a function of mass and metallicity. While $\Delta\Pi_1$ shows no appreciable dependence on the mass, we have found a clear dependence of $\Delta\Pi_1$ on metallicity, which is also supported by predictions from models.

Key words: asteroseismology – stars: evolution – stars: interiors – stars: low-mass.

1 INTRODUCTION

Modelling helium-core-burning (HeCB) low-mass stars has proven to be complicated, given the lack of a detailed physical understanding of how energy and chemical elements are transported in regions adjacent to convectively unstable cores. In particular, this phase is characterized by convective cores that tend to grow with evolution (hence generating sharp chemical profiles), and by the insurgence of a convectively unstable region separated from the core (called helium-semiconvection; Castellani, Giannone & Renzini 1971). Overall, these uncertainties limit our ability to determine precise stellar properties (such as mass and age), which are necessary in the context of studying stellar populations. Moreover, they generate uncertainties in model evolutionary tracks that affect

a wide range of applications, including the theoretical calibration of red clump (RC) stars as distance indicators and the reliability of theoretical predictions about the following evolutionary stages, such as the asymptotic giant branch (AGB) and the WD ones (see e.g. Girardi 2016).

It has been recently recognized that the gravity-mode period spacing ($\Delta\Pi_1$) measured in solar-like oscillating stars provides stringent constraints on core-mixing processes in the HeCB phase (Montalbán et al. 2013; Bossini et al. 2015; Constantino et al. 2015). In our previous work (Bossini et al. 2015, hereafter B15), we investigated how key observational tracers of the near-core properties of HeCB stars (the luminosity of the AGB bump L_{AGBb} and, primarily, $\Delta\Pi_1$) depend on the core-mixing scheme adopted. By comparison with data from Pinsonneault et al. (2014) and Mosser et al. (2012), we concluded, in agreement with independent studies (Constantino et al. 2015), that no standard model can satisfactorily account for the period spacing of HeCB stars. We then proposed a parametrized

★ E-mail: dbossini@bison.ph.bham.ac.uk

model (a moderate penetrative convection, i.e. ∼0.5H_p overshooting with adiabatic stratification in the extra-mixed region; see Section 2) that is able to reproduce at the same time the observed distribution of $\Delta\Pi_1$ and the $L_{\rm AGBb}$. However, we were prevented from drawing any further quantitative conclusions because of the inherent limitation of comparing model predictions against a composite stellar population of less than ∼200 stars, and of potential biases affecting the measurement and detectability of the period spacing (as flagged, for example, in Constantino et al. 2015).

Here, we specifically address these concerns by studying $\Delta\Pi_1$ of RC stars in old open clusters, and by investigating the occurrence of any significant detection bias (Section 3). Moreover, we take a further step and compare our predictions to the more stringent tests provided by analysing the period-spacing structure (Mosser et al. 2014; Vrard, Mosser & Samadi 2016) coupled to spectroscopic constraints, which are now available for thousands of solar-like oscillating giants (SDSS Collaboration et al. 2016), which allows investigating trends of $\Delta\Pi_1$ with mass and metallicity (Section 4).

2 MODELS

We use the stellar evolution code MESA (Paxton et al. 2013) to compute internal structures of stars during the HeCB phase. The default set of physical inputs is described in Rodrigues et al. (2017). We test several types of parametrized mixing schemes during the HeCB phase, which are classified based on the thermal stratification adopted in the region mixed beyond the Schwarzschild border, following the terminology introduced by Zahn (1991). With the term *overshooting* (OV) we refer to models in which the gradient of temperature in such region is radiative ($\nabla_{\rm T,ovHe} = \nabla_r$), while *penetrative convection* (PC) indicates the cases where we assume an adiabatic gradient ($\nabla_{\rm T,ovHe} = \nabla_a$). The size of the extra-mixed region is parametrized as $\alpha_{\rm ovHe}\lambda$, where $\alpha_{\rm ovHe}$ is the OV parameter and $\lambda = \min(H_p, r_{\rm cc})$ is the minimum between one pressure scale-height, H_p, and the radius of the convective core, $r_{\rm cc}$.[1] The mixing schemes tested in this work are as follows:

(i) MOV: $\alpha_{\rm ovHe} = 0.5$, $\nabla_{\rm T,ovHe} = \nabla_r$ (moderate OV),
(ii) MPC: $\alpha_{\rm ovHe} = 0.5$, $\nabla_{\rm T,ovHe} = \nabla_a$ (moderate PC),
(iii) HOV: $\alpha_{\rm ovHe} = 1.0$, $\nabla_{\rm T,ovHe} = \nabla_r$ (high OV),
(iv) HPC: $\alpha_{\rm ovHe} = 1.0$, $\nabla_{\rm T,ovHe} = \nabla_a$ (high PC).

In B15, we tested several of these schemes, and concluded that only MPC (computed using PARSEC; Bressan et al. 2015) was compatible with the observed $\Delta\Pi_1$ and the luminosity distribution in the early AGB. Regarding the large extra-mixing schemes ($\alpha_{\rm ovHe} = 1.0$), we found that only HOV had a good agreement with the observed $\Delta\Pi_1$. However, HOV fails to describe the luminosity distribution (too high $L_{\rm AGBb}$). Finally, the plausibility of a bare-Schwarzschild scheme, here not included, which had already been ruled out theoretically (Gabriel et al. 2014), was also rejected by comparison with observations, including star counts in globular clusters (Cassisi, Salaris & Irwin 2003) and $\Delta\Pi_1$. In contrast to B15, we have modified the mixing scheme in models that develop He-semiconvection zones (MOV, MPC). We prevent the OV region to be (suddenly) attached to the He-semiconvection zone (which in MESA is treated as a convective region), by redefining $r_{\rm cc}$ to the minimum of ∇_r. While this should be considered as an ad hoc treatment with limited

[1] This differs from the default parametrization of OV in MESA, where H_p is instead considered equal to the minimum between $r_{\rm cc}$ and the mixing length $l_{\rm mlt} = \alpha_{\rm mlt}H_p$ (see Deheuvels et al. 2016).
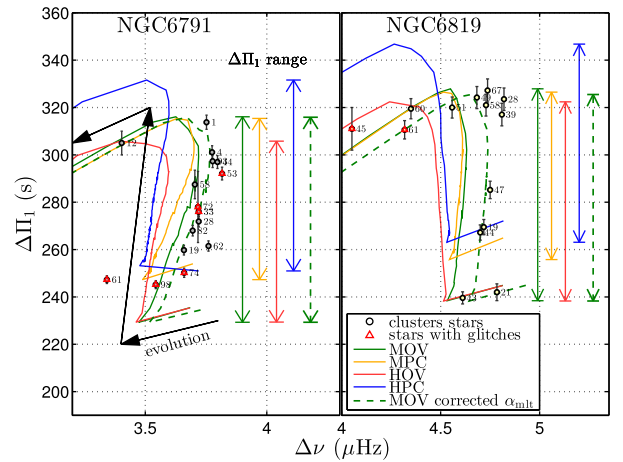

Figure 1. RC stars in NGC 6791 and NGC 6819 in a $\Delta\Pi_1$–$\Delta\nu$ diagram. Model predictions based on different near-core-mixing schemes are shown by solid lines. The vertical lines indicate the range of $\Delta\Pi_1$ covered by each mixing scheme. The dashed line shows MOV models computed with slightly (≲3 per cent) increased mixing-length parameters (compared to the solar-calibrated value). The red triangles mark the presence of buoyancy glitches that, to the first order, induce a modulation in $\Delta\Pi_1$ with respect to the asymptotic value (Miglio et al. 2008; Cunha et al. 2015, and fig. 10 of Mosser et al. 2015), potentially hampering an accurate inference of the asymptotic $\Delta\Pi_1$.

physical significance, it provides a stable numerical scheme and mimics an efficient mixing in the He-semiconvective region. For further details, see Bossini (2016).

3 OLD-OPEN CLUSTERS

Differently from field stars, open clusters are simple stellar populations, i.e. coeval stars with the same initial chemical composition, and a similar mass for their evolved stars. We can therefore perform a stringent test for the proposed mixing schemes in samples free of selection biases due to age, mass and metallicity.

Our observational constraints on RC stars in the old-open clusters NGC 6791 and NGC 6819 are taken from Vrard et al. (2016) and, crucially, include measurements of the gravity-mode period spacing. Among all the stars observed by *Kepler* in NGC 6791 and NGC 6819, we exclude those not belonging to the RC ($\Delta\Pi_1 < 200$ s), stars that are likely to be product of non-single evolution (overmassive/undermassive stars; Handberg et al., submitted), and stars in which, according to Vrard et al. (2016), the signal-to-noise ratio (S/N) is too low for a robust inference on $\Delta\Pi_1$ (five stars in NGC 6819 and three in NGC 6791). The final sample of RC stars in NGC 6819 and NGC 6791 consists of, respectively, 14 and 16 stars (see Tables A1 and A2 for a complete list of targets). To compare data with theoretical predictions, we compute models representative of stars in the RC of the two clusters, adopting different extra-mixing schemes described in Section 2. For NGC 6791, we calculate an evolutionary track with $M = 1.15\,{\rm M_\odot}$, $Z = 0.0350$ and $Y = 0.300$ (Brogaard et al. 2012), while for NGC 6819, we consider models with $M = 1.60\,{\rm M_\odot}$, $Z = 0.0176$ and $Y = 0.267$ (solar metallicity; Handberg et al., submitted). Fig. 1 shows the period spacings of the final samples of the observed RC stars as a function of their average large frequency separation ($\Delta\nu$) and the comparison with our model predictions. $\Delta\nu$ in the models is computed from individual radial-mode frequencies (see Rodrigues et al. 2017). As in B15, the HPC scheme predicts a range of $\Delta\Pi_1$, which is too high
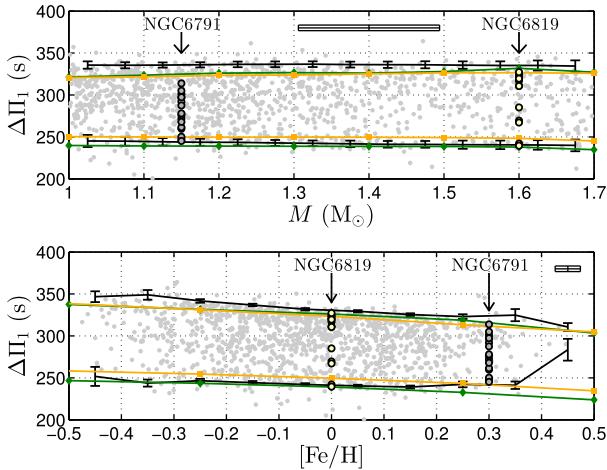
Figure 2. Period spacing of HeCB stars with APOGEE DR13 spectroscopic parameters crossed with Vrard et al. (2016) plotted against mass (upper panel) and metallicity (lower panel). Black lines correspond to the 95th and 5th percentiles of the data distribution along $\Delta\Pi_1$, while green and orange lines represent the model predictions (MOV and MPC schemes, respectively) for $\Delta\Pi_{1,\mathrm{min}}$ and $\Delta\Pi_{1,\mathrm{max}}$. An indication of the typical error on the data is visible in the top right-hand corner of each panel. NGC 6791 (grey dots) and NGC 6819 (yellow dots) cluster stars are also shown.

compared to the observations. The HOV scheme, on the other hand, provides a range that is compatible with the observations; however, it predicts too high a luminosity of the AGB bump. We note that models computed with the OV scheme have an upper limit of $\Delta\Pi_1$ (during the HeCB phase), which does not monotonically increase with α_{ovHe} but rather has a maximum at $\alpha_{\mathrm{ovHe}} \simeq 0.6$. For higher values of α_{ovHe}, the He-semiconvection zone, which develops in the late phases of HeCB, remains separate from the convective core, allowing a larger radiative region, thus effectively decreasing $\Delta\Pi_1$. This is the reason why in Fig. 1 MOV reaches higher $\Delta\Pi_1$ values than HOV.

The comparison between models and stars in NGC 6791 and NGC 6891 supports the conclusions reached in B15, i.e. a moderate extra-mixed scheme reproduces well the maximum $\Delta\Pi_1$ in the HeCB phase. However, while in NGC 6891 the MPC model cannot reach the small period spacings of two stars (21 and 43), which are likely to be early HeCB stars, the moderate overshooting scheme (MOV, green line in Fig. 1) provides a better representation of the data. This model starts the HeCB with a lower $\Delta\Pi_1$, since the OV region is radiative, and reaches $\Delta\Pi_1$ as high as the MPC in the late HeCB, since the overall mixed core has $\nabla_T = \nabla_a$ in both the MOV and the MPC schemes. On the other hand, NGC 6791 does not present early HeCB stars with small $\Delta\Pi_1$, as predicted by the MOV scheme. A possible cause for this may be ascribed to the limited number of stars in the cluster, or to the three RC stars for which $\Delta\Pi_1$ cannot be determined (see Table A2). The tentative evidence for such a discrepancy is supported by the general trend of the lower limit of $\Delta\Pi_1$ with metallicity in field stars (see Section 4 and Fig. 2). However, our sample around the cluster metallicity does not contain a sufficient number of stars to draw strong conclusions.

Offsets in $\Delta\nu$ between models and observations may be attributed to either small differences in the reference mass or to systematic shifts in the effective temperature scale (due to, for example, uncertainties related to near-surface convection and to the outer boundary condition), which modify the predicted photospheric radius, and hence $\Delta\nu$ ($\Delta\nu \propto \sqrt{M/R^3}$). We note that, for the models used in this

study, for example, increasing the solar-calibrated mixing-length parameter by $\lesssim 3$ per cent is sufficient to recover a good agreement (see Fig. 1). We stress that changing the outer boundary conditions/mixing length parameter has no impact on the predictions related to $\Delta\Pi_1$, which is determined by the near-core properties.

4 $\Delta\Pi_1$ OF FIELD STARS

In this section, we explore the effects of mass and metallicity on the asymptotic period spacing of stars in the HeCB phase. The data set we use contains field stars with spectroscopic constraints available from APOGEE DR13 (SDSS Collaboration et al. 2016) and $\Delta\Pi_1$ reported in Vrard et al. (2016). RC stars are selected looking for $\Delta\Pi_1$ greater than 200 s. The range of metallicity considered is [Fe/H] $\in [-0.5, 0.5]$. We limit the mass range to $M_{\mathrm{seism}} \in [1.0, 1.7]\ \mathrm{M}_\odot$ in order to avoid stellar masses that are approaching the secondary clump condition (e.g. see Girardi 1999). Fig. 2 shows the $\Delta\Pi_1$ of the final selection plotted against the mass (upper panel) and metallicity (lower panel). It can be noted that, in the interval considered, the period spacing is limited in a band between a maximum ($\Delta\Pi_{1,\mathrm{max}}$) and a minimum ($\Delta\Pi_{1,\mathrm{min}}$) value. To measure robustly the observed values of $\Delta\Pi_{1,\mathrm{max}}$ and $\Delta\Pi_{1,\mathrm{min}}$, we bin the data set in mass and metallicity, and for each bin, we determine the 95th and 5th percentiles of the $\Delta\Pi_1$ distribution (representing $\Delta\Pi_{1,\mathrm{max}}$ and $\Delta\Pi_{1,\mathrm{min}}$, respectively). In order to evaluate the uncertainties on the percentiles, taking into account also uncertainties on M, $\Delta\Pi_1$ and [Fe/H], we create 1000 realizations of the observed population. We use these to calculate means and standard deviations of $\Delta\Pi_{1,\mathrm{max}}$ and $\Delta\Pi_{1,\mathrm{min}}$, which we then compare to model predictions (see the black lines in Fig. 2).

As evinced from the upper panel of Fig. 2, the data show that the range of $\Delta\Pi_1$ is largely independent of mass, while its upper and lower boundaries decrease with increasing metallicity. To investigate whether models can account for such a behaviour, we compute a small grid of tracks that covers the range of mass and metallicity explored. In the lower panel of Fig. 2, we consider models at different metallicities with mass equal to 1.20 $\mathrm{M}_\odot$ (close to the average mass of ~1.25 $\mathrm{M}_\odot$ of the observed distribution), while for the upper panel, we fix the metallicity to [Fe/H] = 0.00 (mean observed value is [Fe/H] = -0.034) and vary the mass.

We note that models computed with the MOV scheme are in overall good agreement with the observational constraints. $\Delta\Pi_{1,\mathrm{min}}$, which is determined by the initial size of the adiabatically stratified core, is well reproduced by the MOV scheme, suggesting that models with PC are disfavoured at least in the initial phases of HeCB. $\Delta\Pi_{1,\mathrm{max}}$, which depends on the core properties of the much more delicate advanced phases of HeCB, is also in good qualitative agreement with the MOV scheme. Interestingly, models also show decreasing $\Delta\Pi_{1,\mathrm{max}}$ and $\Delta\Pi_{1,\mathrm{min}}$ as metallicity increases. The offset between the observed $\Delta\Pi_{1,\mathrm{max}}$ and the low-mass models (upper panel of Fig. 2) originates primarily from a metallicity effect. Metallicity is not uniformly distributed across the range of masses considered, with small-mass stars being older and hence more metal-poor, while the models shown in the upper panel are computed at fixed Z (solar).

To interpret the behaviour of $\Delta\Pi_{1,\mathrm{max}}$ and $\Delta\Pi_{1,\mathrm{min}}$, it is worth recalling that the asymptotic period spacing of dipolar modes is related to the inverse of the integral of the Brunt–Väisälä frequency (N) over the radius (r) in the g-mode propagation cavity (Tassoul 1980):

$$\Delta\Pi_1 = \frac{2\pi^2}{\sqrt{2}} \left(\int_{r_1}^{r_2} \frac{N}{r}\,\mathrm{d}r \right)^{-1}. \tag{1}$$
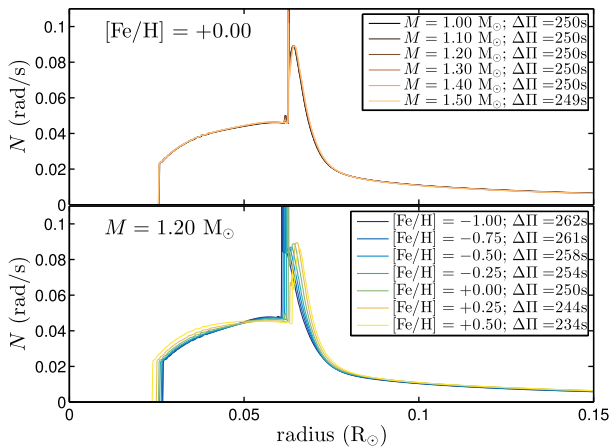
Figure 3. Brunt–Väisälä frequency in the model grid presented in Rodrigues et al. (2017) at the start of the helium burning. N profiles are shown in the upper panel for models with fixed metallicity ([Fe/H] = 0.00), while in the lower panel, they are shown for fixed mass ($M = 1.20\,\mathrm{M_\odot}$).

The region that mostly influences the integral in equation (1) is the radiative region near the centre (due to the dependence on $1/r$). Since N is typically null in the deep fully convective regions, larger convective cores will lead to larger values of $\Delta\Pi_1$ (Montalbán et al. 2013). Looking at the Brunt–Väisälä frequency at the very beginning of the HeCB phase (Fig. 3), we note that for a fixed metallicity, all the profiles overlap, while visible differences are found by changing the metallicity. The reason behind this has to be searched in the mass of the helium-rich core (M_{He}) at the beginning of HeCB, which determines the physical conditions of the central regions. M_{He} is similar to the critical mass $M_{\mathrm{He,0}}$, which is needed for the plasma to reach temperatures high enough to burn helium and start the helium flash. For stars with masses in our range of interest, the critical mass $M_{\mathrm{He,0}}$ is the result of two competing mechanisms along the red giant branch (RGB): the central cooling due to the degeneracy and the hydrogen-burning shell that constantly deposits helium on the core. While the first is independent of metallicity, the second has an efficiency that increases with Z. The final effect tends to decrease $M_{\mathrm{He,0}}$ with increasing Z (Cassisi & Salaris 2013). Indeed, the different $M_{\mathrm{He,0}}$ and its properties influence the H-burning shell efficiency also in the HeCB phase, leading to high-Z stars having a more efficient H-burning shell, which contributes more to the total luminosity than in the low-Z stars. Therefore, in more metal rich stars, the contribution of the HeCB to the whole energy budget is lower than in metal-poor ones. This occurrence has the consequence that metal-rich stars develop a smaller convective core – and hence smaller $\Delta\Pi_1$ – with respect to low-Z stars. On the other hand, low-mass stars with the same Z end up with similar $M_{\mathrm{He,0}}$ and therefore a similar helium core during the HeCB and similar $\Delta\Pi_1$. However, this is true only for $M \lesssim 1.5$–$1.7\,\mathrm{M_\odot}$ (depending on Z). Above this value, $M_{\mathrm{He,0}}$ starts to decrease since we approach the secondary clump (the degeneracy of the He core decreases and hence $M_{\mathrm{He,0}}$; Girardi 1999).

An additional test is made to quantify the effect of the initial helium on $\Delta\Pi_1$. In our grid, Y is in fact coupled with Z via a linear chemical enrichment relation (see Rodrigues et al. 2017). To decouple the effect of Z and Y, we compute five tracks of mass $1.50\,\mathrm{M_\odot}$ and $Z = 0.031$ ([Fe/H] = 0.25), but with initial helium $Y = 0.25$, 0.28, 0.30, 0.35 and 0.40 (with $Y = 0.28$ as our default value). Fig. 4, right-hand panel, shows the evolution of $\Delta\Pi_1$ with central helium for the five tracks. We note that the effect on
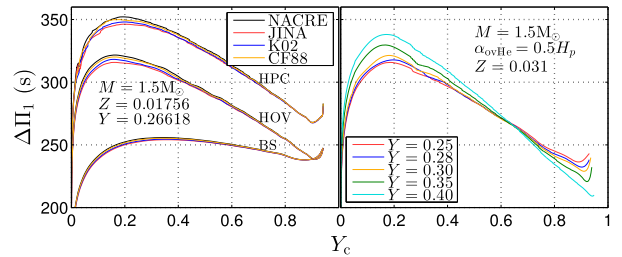
Figure 4. Left-hand panel: RC-$\Delta\Pi_1$ evolution as a function of central helium mass of an $M = 1.50\,\mathrm{M_\odot}$ solar metallicity star with three different mixing schemes and four different $^{12}\mathrm{C}(\alpha,\gamma)^{16}\mathrm{O}$ reaction rates. Right-hand panel: RC-$\Delta\Pi_1$ evolution as a function of central helium mass fraction of an $M = 1.50\,\mathrm{M_\odot}$ star computed assuming three different combinations of Z and Y.

$\Delta\Pi_{1,\mathrm{max}}$ and $\Delta\Pi_{1,\mathrm{min}}$ grows linearly with Y. However, for a variation of $\Delta Y = {\sim}0.02$ from the default value ($Y = 0.25$ and 0.30), the deviation on $\Delta\Pi_{1,\mathrm{max}}$ ($\Delta\Pi_{1,\mathrm{min}}$) lies within the observed uncertainty on $\Delta\Pi_1$ (${\sim}3$–4 s). The deviation we tested is compatible with typical spread on disc populations (Casagrande et al. 2007). Nevertheless, the effect becomes substantial for extreme enrichments, for example, in bulge or globular clusters where populations with very different He abundances and the same metallicity may coexist (Renzini et al. 2015).

5 ADDITIONAL UNCERTAINTIES ON $\Delta\Pi_1$: $^{12}\mathrm{C}(\alpha,\gamma)^{16}\mathrm{O}$ NUCLEAR REACTION RATE

As shown above, $\Delta\Pi_1$ is strongly dependent on assumptions related to core convection and metallicity; however, additional parameters and uncertainties may also have impact on $\Delta\Pi_1$, in particular the $^{12}\mathrm{C}(\alpha,\gamma)^{16}\mathrm{O}$ reaction rate, which, along with triple-α, plays a fundamental role, especially at the end of the HeCB (e.g. see Cassisi et al. 2003; Straniero et al. 2003; Constantino et al. 2015).

We compute a series of HeCB evolutionary tracks ($M = 1.5\,\mathrm{M_\odot}$, solar abundance) in which we adopt four $^{12}\mathrm{C}(\alpha,\gamma)^{16}\mathrm{O}$ reaction rates in conjunction with three mixing schemes: Bare–Schwarzschild model (BS), $1.0H_{\mathrm{p}}$ step function overshooting (HOV) and $1H_{\mathrm{p}}$ penetrative convection (HPC). The $^{12}\mathrm{C}(\alpha,\gamma)^{16}\mathrm{O}$ reaction rates considered are the tabulated values given by JINA (Cyburt et al. 2010), K02 (Kunz et al. 2002), CF88 (Caughlan & Fowler 1988) and NACRE (Angulo et al. 1999), and already made available in MESA. While no difference can be noted at the beginning of the phase, the impact of the different mixing schemes is evident at the maximum period spacing (end of the HeCB), where HOV tracks show a scatter of around 6–7 s between them, compared to only ${\sim}2$ s for BS (Fig. 4). We therefore expect an uncertainty between 6 and 2 s on the MPC and MOV models. This value is comparable with the observed average $\Delta\Pi_1$ uncertainty for clump stars (${\sim}4$ s).

6 DISCUSSION AND CONCLUSION

The precise measurements of gravity-mode period spacing ($\Delta\Pi_1$) in thousands of HeCB stars have opened the door to detailed studies of the near-core structure of such stars, which had not been possible before (Montalbán et al. 2013; B15; Constantino et al. 2015).

Here, we provide additional stringent tests of the mixing schemes by stress testing the models presented in B15 against results on the simple population of RC stars belonging to the old-open

clusters monitored by *Kepler*, and making use of the updated precise inference on $\Delta\Pi_1$ presented by Vrard et al. (2016) coupled with spectroscopic constraints from APOGEE DR13 (SDSS Collaboration et al. 2016).

We find that in clusters $\Delta\Pi_1$ is measured in all RC stars with a few exceptions (as discussed in Section 3, Tables A1 and A2), and that models with moderate overshooting can reproduce the range of period spacing observed. In particular, our models do not support the need to extend the size of the adiabatically stratified core, at least at the beginning of the HeCB phase. This conclusion is based primarily on ensemble studies of $\Delta\Pi_1$ as a function of mass and metallicity, where we could also show that models successfully reproduce the main trends (or their absence). While $\Delta\Pi_1$ shows no appreciable dependence on the mass, we have found a clear dependence of $\Delta\Pi_1$ on metallicity (Fig. 2) also shown by the models, which strengthens even further the result on the clusters. We complement the study by considering how theoretically predicted $\Delta\Pi_1$ depends on the initial helium mass fraction and on the nuclear cross-sections adopted in the models, and conclude that the adopted mixing scheme and metallicity are the dominant effects.

The parametrized model presented here should be considered as a first approximation that broadly reproduces the inferred average asymptotic period spacing. Significant improvements can be made by looking at signatures of sharp-structure variations (B15; Cunha et al. 2015; Mosser et al. 2015), which will enable to test in greater detail the chemical and temperature stratification near the edge of the convective core, providing additional indications that will eventually be compared with more realistic and physically justified models of convection in this key stellar evolutionary phases.

ACKNOWLEDGEMENTS

REFERENCES

Angulo C. et al., 1999, Nucl. Phys. A, 656, 3
Bossini D., 2016, PhD thesis, Univ. Birmingham
Bossini D. et al., 2015, MNRAS, 453, 2290 (B15)
Bressan A., Girardi L., Marigo P., Rosenfield P., Tang J., 2015, Astrophys. Space Sci. Proc., 39, 25
Brogaard K. et al., 2012, A&A, 543, A106
Casagrande L., Flynn C., Portinari L., Girardi L., Jimenez R., 2007, MNRAS, 382, 1516
Cassisi S., Salaris M., 2013, Old Stellar Populations: How to Study the Fossil Record of Galaxy Formation
Cassisi S., Salaris M., Irwin A. W., 2003, ApJ, 588, 862
Castellani V., Giannone P., Renzini A., 1971, Ap&SS, 10, 355
Caughlan G. R., Fowler W. A., 1988, At. Data Nucl. Data Tables, 40, 283
Constantino T., Campbell S. W., Christensen-Dalsgaard J., Lattanzio J. C., Stello D., 2015, MNRAS, 452, 123
Cunha M. S., Stello D., Avelino P. P., Christensen-Dalsgaard J., Townsend R. H. D., 2015, ApJ, 805, 127
Cyburt R. H. et al., 2010, ApJS, 189, 240
Deheuvels S., Brandão I., Silva Aguirre V., Ballot J., Michel E., Cunha M. S., Lebreton Y., Appourchaux T., 2016, A&A, 589, A93
Gabriel M., Noels A., Montalbán J., Miglio A., 2014, A&A, 569, A63
Girardi L., 1999, MNRAS, 308, 818
Girardi L., 2016, ARA&A, 54, 95
Kunz R., Fey M., Jaeger M., Mayer A., Hammer J. W., Staudt G., Harissopulos S., Paradellis T., 2002, ApJ, 567, 643
Miglio A., Montalbán J., Noels A., Eggenberger P., 2008, MNRAS, 386, 1487
Montalbán J., Miglio A., Noels A., Dupret M.-A., Scuflaire R., Ventura P., 2013, ApJ, 766, 118
Mosser B. et al., 2012, A&A, 540, A143
Mosser B. et al., 2014, A&A, 572, L5
Mosser B., Vrard M., Belkacem K., Deheuvels S., Goupil M. J., 2015, A&A, 584, A50
Paxton B. et al., 2013, ApJS, 208, 4
Pinsonneault M. H. et al., 2014, ApJS, 215, 19
Renzini A. et al., 2015, MNRAS, 454, 4197
Rodrigues T. S. et al., 2017, MNRAS, 467, 1433
SDSS Collaboration et al., 2016, ApJS, preprint (arXiv:1608.02013)
Stello D. et al., 2011, ApJ, 739, 13
Straniero O., Domínguez I., Imbriani G., Piersanti L., 2003, ApJ, 583, 878
Tassoul M., 1980, ApJS, 43, 469
Vrard M., Mosser B., Samadi R., 2016, A&A, 588, A87
Zahn J.-P., 1991, A&A, 252, 179

APPENDIX

Table A1. NGC 6819 stellar catalogue. Stellar classes were chosen considering the classification in Stello et al. (2011) and $\Delta\Pi_1$, $\Delta\nu$, and ν_{max} in Vrard et al. (2016).

N	KIC	ν_{max} (μHz)	$\Delta\nu$ (μHz)	$\Delta\Pi_1$ (s)	$\sigma_{\Delta\Pi_1}$ (s)	Vrard et al. (2016)	Class	Selected RC stars	Notes
1	4937011	–	–	–	–	–	RGB	–	
2	4937056	46.10	4.76	–	–	Yes	Unclear	–	Low $l = 1$ structure
3	4937257	–	–	–	–	–	RGB	–	
4	4937576	32.95	3.56	–	–	Yes	RGB	–	
5	4937770	94.30	7.83	160.70	1.99	Yes	Unclear	–	Possible second clump
6	4937775	89.92	7.33	226.50	4.61	Yes	Unclear	–	Little $l = 1$ structure. No photometric clump
7	5023732	27.08	3.12	–	–	Yes	RGB	–	
8	5023845	109.94	8.96	–	–	Yes	RGB	–	
9	5023889	–	–	–	–	–	RGB	–	
10	5023931	50.57	4.92	–	–	Yes	RGB	–	Little $l = 1$ structure
11	5023953	48.75	4.74	299.00	4.36	Yes	RC	No	$M_{seismo} = 1.83\,M_\odot$

Table A1 – *continued*

N	KIC	ν_{max} (μHz)	$\Delta\nu$ (μHz)	$\Delta\Pi_1$ (s)	$\sigma_{\Delta\Pi_1}$ (s)	Vrard et al. (2016)	Class	Selected RC stars	Notes
12	5024043	55.98	5.64	61.00	2.00	Yes	RGB	–	
13	5024143	122.84	9.68	68.40	6.59	Yes	RGB	–	
14	5024240	153.85	12.00	–	–	Yes	RGB	–	
15	5024268	–	–	–	–	–	RGB	–	
16	5024272	–	–	–	–	–	RGB	–	
17	5024297	46.24	4.60	–	–	Yes	RGB	–	
18	5024312	96.68	8.13	–	–	Yes	RGB	–	
19	5024327	44.18	4.72	269.50	3.21	Yes	RC	Yes	
20	5024329	–	–	–	–	–	RGB	–	
21	5024404	47.09	4.78	242.00	3.54	Yes	RC	Yes	
22	5024405	98.89	8.29	–	–	Yes	RGB	–	
23	5024414	78.17	6.46	280.70	6.16	Yes	RC	No	$M_{\mathrm{seismo}} = 2.63\,\mathrm{M_\odot}$
24	5024456	3.86	0.70	–	–	Yes	RGB	–	
25	5024476	65.94	5.74	298.00	3.79	Yes	RC	No	$M_{\mathrm{seismo}} = 2.38\,\mathrm{M_\odot}$
26	5024512	72.97	6.70	–	–	Yes	RGB	–	
27	5024517	50.13	4.94	319.20	5.11	Yes	RGB	–	Non-photometric member
28	5024582	46.30	4.82	323.50	4.76	Yes	RC	Yes	
29	5024583	37.89	3.91	–	–	Yes	RGB	–	
30	5024601	32.30	3.68	–	–	Yes	RC	–	Very low $l = 1$
31	5024750	12.74	1.80	–	–	Yes	RGB	–	
32	5024851	4.06	0.75	–	–	Yes	RGB	–	
33	5024870	–	–	–	–	–	RGB	–	
34	5024967	44.97	4.71	–	–	Yes	RC	–	Very low $l = 1$
35	5024984	–	–	–	–	–	RGB	–	
36	5111718	135.49	10.59	87.53	1.06	Yes	RGB	–	
37	5111820	–	–	–	–	–	RGB	–	
38	5111940	52.79	5.20	–	–	Yes	RGB	–	
39	5111949	47.35	4.81	317.00	4.76	Yes	RC	Yes	
40	5112072	125.27	10.08	92.40	0.91	Yes	RGB	–	
41	5112288	46.94	4.77	–	–	Yes	RC	No	Very low $l = 1$
42	5112361	67.63	6.19	91.40	0.90	Yes	RGB	–	
43	5112373	43.84	4.61	239.60	2.57	Yes	RC	Yes	
44	5112387	44.91	4.70	267.20	3.21	Yes	RC	Yes	
45	5112401	36.50	4.05	311.00	9.00	Yes	RC	Yes	Presence of glitch
46	5112403	141.73	11.18	86.80	1.07	Yes	RGB	–	
47	5112467	45.15	4.75	285.20	3.67	Yes	RC	Yes	
48	5112481	5.18	0.92	–	–	Yes	RGB	–	
49	5112491	44.25	4.68	324.20	4.65	Yes	RC	Yes	
50	5112558	–	–	–	–	–	RGB	–	
51	5112730	43.60	4.56	320.00	4.46	Yes	RC	Yes	
52	5112734	40.65	4.16	–	–	Yes	RGB	–	
53	5112741	–	–	–	–	–	RGB	–	
54	5112744	43.97	4.44	–	–	Yes	RGB	–	
55	5112751	1.32	0.39	–	–	Yes	RC	No	Very low $l = 1$
56	5112786	7.70	1.17	–	–	Yes	RGB	–	
57	5112880	25.43	2.82	–	–	Yes	RGB	–	
58	5112938	44.54	4.73	321.00	4.59	Yes	RC	Yes	
59	5112948	42.28	4.31	–	–	Yes	RGB	–	
60	5112950	41.59	4.35	319.50	4.26	Yes	RC	Yes	
61	5112974	40.08	4.32	310.60	3.87	Yes	RC	Yes	Presence of glitch
62	5113041	37.13	4.01	–	–	Yes	RGB	–	
63	5113061	4.53	0.84	–	–	Yes	RGB	–	
64	5113441	154.68	11.76	89.65	1.24	Yes	RGB	–	
65	5199859	0.70	0.15	–	–	Yes	RGB	–	
66	5200088	–	–	–	–	–	RGB	–	
67	5200152	45.71	4.74	327.20	4.89	Yes	RC	Yes	

Table A2. NGC 6791 stellar catalogue. Stellar classes were chosen considering the classification in Stello et al. (2011) and $\Delta\Pi_1$, $\Delta\nu$, and ν_{max} in Vrard et al. (2016).

N	KIC	ν_{max} (μHz)	$\Delta\nu$ (μHz)	$\Delta\Pi_1$ (s)	$\sigma_{\Delta\Pi_1}$ (s)	Vrard et al. (2016)	Class	Selected RC stars	Notes
1	2297384	30.49	3.75	313.78	3.00	Yes	RC	Yes	
2	2297574	–	–	–	–	–	RGB	–	
3	2297793	–	–	–	–	–	RGB	–	
4	2297825	30.43	3.77	301.10	2.76	Yes	RC	Yes	
5	2298097	–	–	–	–	–	RGB	–	
6	2435987	38.07	4.22	–	–	Yes	RGB	–	
7	2436097	42.06	4.54	–	–	Yes	RGB	–	
8	2436209	57.01	5.76	67.30	2.46	Yes	RGB	–	
9	2436291	–	–	–	–	–	RGB	–	
10	2436332	28.29	3.40	–	–	Yes	RGB	–	
11	2436376	–	–	–	–	–	RGB	–	
12	2436417	27.07	3.40	305.00	5.00	Yes	RC	Yes	
13	2436458	37.08	4.17	–	–	Yes	RGB	–	
14	2436540	57.76	5.83	–	–	Yes	RGB	–	
15	2436593	24.96	3.56	–	–	Yes	RGB	–	Binary star
16	2436676	131.86	11.35	80.60	1.16	Yes	RGB	–	
17	2436688	76.01	7.28	–	–	Yes	RGB	–	
18	2436715	–	–	–	–	–	RGB	–	
19	2436732	30.27	3.66	259.76	2.04	Yes	RC	Yes	
20	2436759	32.63	3.73	–	–	Yes	RGB	–	
21	2436804	–	–	–	–	–	RGB	–	
22	2436814	24.51	3.13	–	–	Yes	RGB	–	
23	2436818	97.32	8.84	76.10	0.56	Yes	RGB	–	
24	2436824	34.03	3.87	–	–	Yes	RGB	–	
25	2436842	–	–	–	–	–	RGB	–	
26	2436900	35.62	4.07	–	–	Yes	RGB	–	
27	2436912	29.79	3.73	–	–	Yes	RC	No	Suppressed $l = 1$
28	2436944	30.86	3.72	271.90	2.28	Yes	RC	Yes	
29	2436954	34.48	4.16	–	–	Yes	RGB	–	
30	2436981	–	–	–	–	–	RGB	–	
31	2437033	–	–	–	–	–	RGB	–	
32	2437040	25.49	3.08	–	–	Yes	RGB	–	
33	2437103	28.46	3.72	276.00	2.17	Yes	RC	Yes	Presence of glitch
34	2437112	–	–	–	–	–	RGB	–	
35	2437171	–	–	–	–	–	RGB	–	
36	2437178	–	–	–	–	–	RGB	–	
37	2437209	–	–	–	–	–	RGB	–	
38	2437240	45.56	4.86	63.60	1.68	Yes	RGB	–	
39	2437261	–	–	–	–	–	RGB	–	
40	2437270	69.36	6.54	62.60	2.75	Yes	RGB	–	
41	2437296	–	–	–	–	–	RGB	–	
42	2437325	93.60	8.54	75.30	0.53	Yes	RGB	–	
43	2437340	8.44	1.30	–	–	Yes	RGB	–	
44	2437353	31.25	3.80	297.00	2.73	Yes	RC	Yes	
45	2437394	159.70	12.99	–	–	Yes	RGB	–	
46	2437402	46.41	4.84	–	–	Yes	RGB	–	
47	2437413	–	–	–	–	–	RGB	–	
48	2437443	–	–	–	–	–	RGB	–	
49	2437444	18.83	2.48	–	–	Yes	RGB	–	
50	2437488	64.77	6.30	–	–	Yes	RGB	–	
51	2437496	4.43	0.86	–	–	Yes	RGB	–	
52	2437507	20.41	2.62	–	–	Yes	RGB	–	
53	2437564	32.02	3.82	292.10	2.69	Yes	RC	Yes	Presence of glitch
54	2437589	46.11	4.63	–	–	Yes	Unclear	–	Uncertain $\Delta\Pi_1$, probably RGB.
55	2437624	–	–	–	–	–	RGB	–	
56	2437630	–	–	–	–	–	RGB	–	
57	2437653	74.58	7.07	–	–	Yes	RGB	–	
58	2437698	29.78	3.70	287.50	6.01	Yes	RC	Yes	
59	2437781	85.46	7.88	–	–	Yes	RGB	–	
60	2437792	–	–	–	–	–	RGB	–	
61	2437804	26.71	3.34	247.30	1.63	Yes	RC	Yes	
62	2437805	31.93	3.76	261.50	2.16	Yes	RC	Yes	
63	2437816	17.78	2.37	–	–	Yes	RGB	–	

Table A2 *– continued*

N	KIC	ν_{max} (μHz)	$\Delta\nu$ (μHz)	$\Delta\Pi_1$ (s)	$\sigma_{\Delta\Pi_1}$ (s)	Vrard et al. (2016)	Class	Selected RC stars	Notes
64	2437851	12.37	1.90	–	–	Yes	RGB	–	
65	2437897	–	–	–	–	–	RGB	–	
66	2437930	–	–	–	–	–	RGB	–	
67	2437933	107.46	9.45	76.80	0.63	Yes	RGB	–	
68	2437957	93.15	8.57	–	–	Yes	RGB	–	
69	2437965	7.20	1.28	–	–	Yes	RGB	–	
70	2437972	85.43	7.89	69.10	0.41	Yes	RGB	–	
71	2437976	89.62	8.21	75.50	0.51	Yes	RGB	–	
72	2437987	29.95	3.72	278.00	15.00	Yes	RC	Yes	Presence of glitch
73	2438038	62.25	6.18	66.40	2.65	Yes	RGB	–	
74	2438051	30.46	3.66	250.20	1.93	Yes	RC	Yes	Presence of glitch
75	2438053	–	–	–	–	–	RGB	–	
76	2438140	70.96	6.79	67.30	3.20	Yes	RGB	–	
77	2438192	–	–	–	–	–	RGB	–	
78	2438333	61.09	6.11	65.00	2.48	Yes	RGB	–	
79	2438421	0.67	0.21	–	–	Yes	RGB	–	
80	2568519	–	–	–	–	–	RGB	–	
81	2568916	0.45	0.23	–	–	Yes	RC	No	Very poor S/N
82	2569055	30.49	3.69	268.00	2.22	Yes	RC	Yes	
83	2569126	–	–	–	–	–	RGB	–	
84	2569360	21.32	2.76	–	–	Yes	RGB	–	
85	2569488	0.54	0.23	–	–	Yes	RC	No	Very poor S/N
86	2569618	56.41	5.70	–	–	Yes	RGB	–	
87	2569650	–	–	–	–	–	RGB	–	
88	2569673	–	–	–	–	–	RGB	–	
89	2569712	–	–	–	–	–	RGB	–	
90	2569752	–	–	–	–	–	RGB	–	
91	2569912	–	–	–	–	–	RGB	–	
92	2569935	5.20	0.98	–	–	Yes	RGB	–	
93	2569945	30.13	3.78	297.30	2.66	Yes	RC	Yes	
94	2570094	67.83	6.55	71.05	0.34	Yes	RGB	–	
95	2570134	–	–	–	–	–	RGB	–	
96	2570144	–	–	–	–	–	RGB	–	
97	2570172	75.15	7.09	–	–	Yes	RGB	–	
98	2570214	28.05	3.54	245.20	1.69	Yes	RC	Yes	Presence of glitch
99	2570244	105.70	9.28	76.85	0.62	Yes	RGB	–	
100	2570263	–	–	–	–	–	RGB	–	
101	2570384	47.54	4.84	–	–	Yes	RGB	–	
102	2570518	46.45	4.98	–	–	Yes	RGB	–	
103	2570519	–	–	–	–	–	RGB	–	
104	2579142	–	–	–	–	–	RGB	–	
105	2582664	–	–	–	–	–	RGB	–	
106	2585397	–	–	–	–	–	RGB	–	

This paper has been typeset from a TEX/LATEX file prepared by the author.